Drop-in additives for suspension manipulation: Colloidal motion induced by sedimenting soluto-inertial beacons

Anirudha Banerjee, Huanshu Tan, and Todd M. Squires
Department of Chemical Engineering, University of California, Santa Barbara, California 93106-5080, USA

(Received 9 January 2020; accepted 8 May 2020; published 2 July 2020)

Soluto-inertial (SI) suspension interactions involve nonequilibrium colloidal migration over millimeters, driven by "beacons" that establish long-lasting chemical gradients. Previous demonstrations of the SI concept were restricted to fixed, cylindrical beacons that would sustain solute fluxes in controlled two-dimensional geometries. Here we examine soluto-inertial interactions established by a spherical beacon that sediments through a suspension. The sedimenting beacon leaves a trailing solute wake, the flux from which drives the motion of neighboring suspended objects. Experiments reveal wakes that can attract or repel particles, depending on the solute-colloid pair, creating local regions in the suspension that are enriched in or devoid of particles. Theoretical descriptions accurately capture experimental observations and provide predictive ability to gauge the strength of these interactions in terms of the design parameters. We anticipate that long-range, bulk suspension interactions driven by "drop-in" beacon additives will enable on-demand flocculation of dilute suspensions and separation of colloidal mixtures.

DOI: 10.1103/PhysRevFluids.5.073701

I. INTRODUCTION

Suspensions of micron sized particles find application in a variety of applications of industrial and technological relevance (e.g., food, cosmetics, inks, paints, vaccines, three-dimensional (3D) printing, and soft robotics [1–6]). The ability to tune interactions between suspended objects enables users to control suspension performance, stability, and overall behavior. Equilibrium suspension interactions, however, are typically limited to less than 1 μm in water [7], thereby limiting the capacity to design suspension behavior.

Recent decades have seen a resurgence of interest in "physicochemical hydrodynamics," a term coined by Levich [8] to describe fluidic systems in which chemical effects (like solute fluxes, physical and chemical adsorption, and homogeneous and heterogeneous reactions) couple with mechanical forces and stresses to drive fluid flows and particulate motion. Recent reviews describe a wealth of recent work on the physicochemical hydrodynamics of drops and bubbles [9], and specifically on diffusiophoresis [10,11], as is particularly relevant to this work.

We recently introduced nonequilibrium soluto-inertial (SI) interactions that can last thousands of seconds and extend many orders of magnitude farther than typical equilibrium interactions [12–14]. These SI interactions require three key ingredients: (i) an SI beacon that establishes and maintains a long-lasting solute flux, (ii) particles that respond to the flux and migrate via diffusiophoresis (DP), and (iii) a solute that mediates the interaction. The term "soluto-inertia" was chosen by analogy with thermal inertia, where high heat capacity objects in poor heat transfer media respond slowly to changes in local temperature, and therefore maintain long-lasting heat flux.

The sign of the SI interaction (i.e., attractive or repulsive) depends on the direction particles migrate diffusiophoretically in response to the solute flux, which in turn depends on interactions between the solute and the surface chemistry of the colloid. Attractive interactions between the solute and colloidal surface cause diffusiophoretic migration up concentration gradients of that solute [15,16]. With such solute-colloid pairs, the solute wake released by a sedimenting SI beacon

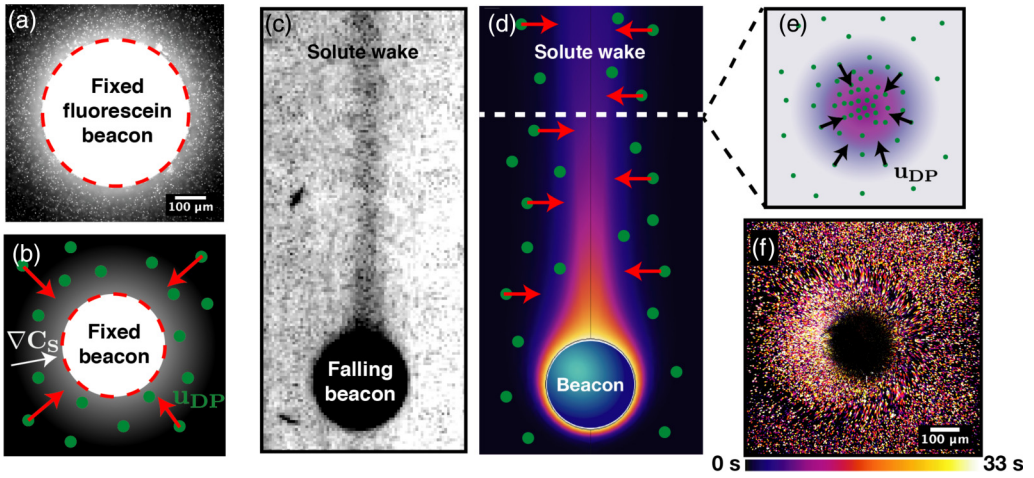

FIG. 1. Freely falling SI beacons induce diffusiophoretic colloidal migration. (a) A cylindrical beacon post fixed within a microfluidic chamber establishes a radial concentration profile of fluorescein. (b) The solute flux driven by a fixed cylindrical beacon drives suspended colloids to migrate diffusiophoretically in the radial direction. (c) Experimental visualization and (d) computed profile of solute emitted by a sedimenting beacon, which forms a convection-diffusion boundary layer along the beacon and a solute wake behind. The experiment (c) comprises a water drop unloading Oil Red O dye as it sediments through an oil bath. (e) As the solute in the wake diffuses radially outward, its concentration gradients drive suspended particles to migrate toward (or away) from the wake, creating regions in the suspension that are enriched or depleted in particles. (f) SI attraction of fluorescent colloids by a solute wake trailing a sedimenting beacon, illuminated from the side by a laser sheet and visualized from below. Color-coded streak lines show diffusiophoretic migration directed toward the center of the dark circle, which arises because the sedimenting beacon physically blocks the camera's view.

attracts suspended colloids, so that particle concentration in the wake N_{SI} exceeds the background concentration N_0. If, on the other hand, interactions between the solute and colloid surface are repulsive, then colloids move diffusiophoretically down solute concentration gradients, away from the solute wake, to create a depletion region in the suspension ($N_{\mathrm{SI}} < N_0$).

Our previous work focused on cylindrical beacons that are fixed in place, that initiate and sustain colloidal migration in well-controlled microfluidic geometries [Figs. 1(a) and 1(b)]. Here we focus on freely sedimenting spherical beacons that drive SI interactions within the surrounding suspension.

In particular, we consider SI beacons whose density and size [$\mathcal{O}(100\ \mu\mathrm{m})$] is large enough to cause them to sediment through the suspension. Solute released by sedimenting beacons forms convection-diffusion boundary layers along the beacon, leaving a wake at high-enough Peclet number [Figs. 1(c) and 1(d)], as described below. Solute within the wake subsequently diffuses out radially, creating a concentration gradient that initiates DP attraction or repulsion of suspended objects [Figs. 1(e) and 1(f)].

We present both experimental demonstrations and theoretical descriptions of the solute wake formation, including scaling arguments to capture the effect of the falling velocity and the beacon size on the mass of solute left behind the sedimenting beacon. Finally, we identify the design parameters that govern the particle response to the solute flux emanating from the wake, and map out parameter space with the goal of facilitating the predictive design of SI systems.

II. EXPERIMENTS

Spherical beacons of radius $R_B = 0.2$–0.5 mm are prepared as described in Sec. IV B and dropped into a suspension of negatively charged PS particles dispersed in a glycerol-water solution.

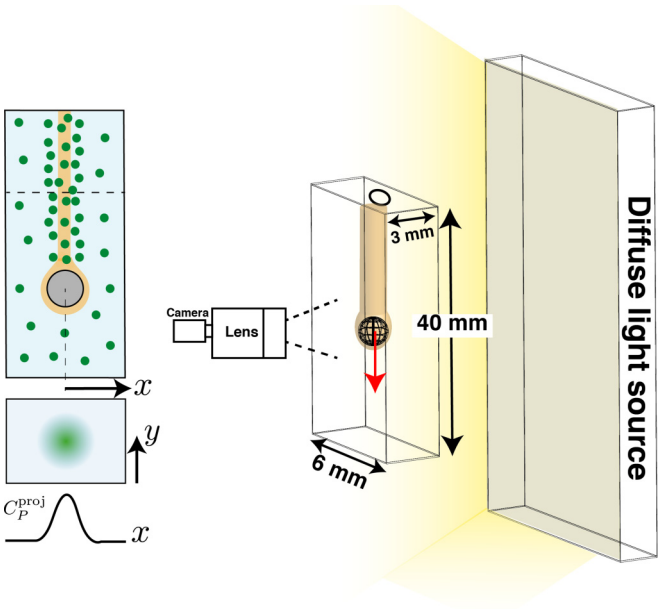

FIG. 2. The experimental setup used to record the transmitted light intensity through a suspension of negatively charged polystyrene colloids. A uniform, diffuse white light source is held behind the sample cell containing the suspension. The sample cell itself is 40 mm tall, 6 mm wide, and 3 mm thick, with acrylic side walls. The front, back, and top of the cell are enclosed with glass slides. A hole drilled through the top slide provides access into the cell. A charge-coupled device (CCD) camera attached to a zoom lens is used to record images of the experimental setup at 10 frames per second.

A 24% glycerol–76% water mixture ($\mu = 3$ cP, $\rho = 1.08$ g/cm^3, $\nu = 3 \times 10^{-2}$ cm^2/s) [17] is prepared to increase the viscosity of the continuous phase and suppress convective fluctuations. Bright-field images are recorded from the side using a CCD camera and zoom lens, while illuminating the sample cell from behind (Fig. 2), so that relatively dark regions indicate higher particle concentrations and vice versa.

Experiments are performed with two distinct kinds of beacons: (i) ionogel beacons that are loaded with the ionic liquid 1-*n*-butyl-3-methylimidazolium iodide ([C_4mim][I]) and (ii) beacons loaded with the anionic surfactant sodium dodecyl sulfate (SDS). Previously, fixed cylindrical ionogel beacons releasing [C_6mim][I] were shown to attract negatively charged polystyrene (PS) colloids, whereas fixed beacons emitting SDS repelled them [13].

The sedimentation velocity of beacons in the Stokes flow limit (Re < 1) is given by [18]

$$U_B = \frac{2}{9}\frac{\Delta\rho g R_B^2}{\mu}, \tag{1}$$

where $\Delta\rho = \rho_B - \rho_f$ is the difference in density of the beacon (ρ_B) and the fluid (ρ_f), μ is the fluid viscosity, and g is the acceleration due to gravity. The Reynolds and Peclet numbers for freely falling beacons in Stokes flow, Re and Pe, can simply be expressed in terms of the size of the sedimenting beacon

$$\mathrm{Re} = \frac{\rho_f U_B R_B}{\mu} \propto R_B^3, \tag{2}$$

$$\mathrm{Pe} = \frac{U_B R_B}{D_S} \propto R_B^3. \tag{3}$$

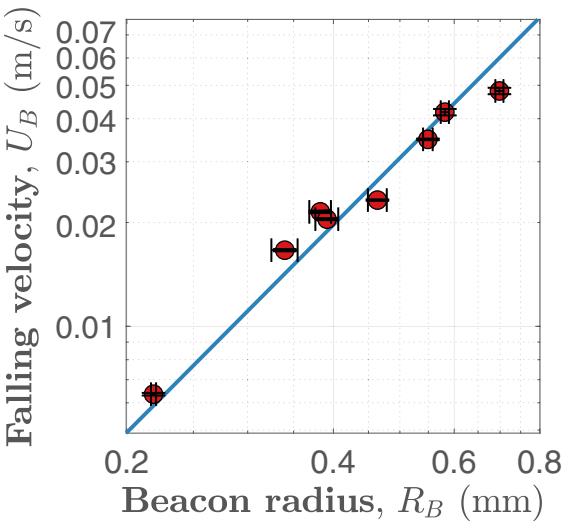

FIG. 3. The falling velocity of ionogel beacons of different sizes. Points correspond to velocities and radii measured experimentally, while the solid line represents the prediction of Eq. (1). Error bars show standard deviations in the measured velocities and radii.

Reynolds numbers for beacons in the SI experiments described below range from 0.1 to 1, and Peclet numbers range from 10^3 to 10^4. The largest beacons, used only in the sedimentation velocity measurements in Fig. 3, have Re ~ 10. Even though the Reynolds number is typically small, the Peclet number is large since the Schmidt number,

$$\mathrm{Sc} = \frac{\mathrm{Pe}}{\mathrm{Re}} = \frac{\nu}{D_S}, \tag{4}$$

is also large. Here D_S and ν are diffusion coefficients for the solute and the fluid momentum, respectively. The Schmidt number therefore captures how much more quickly momentum, or vorticity, diffuses than the solute and is generally large for solutes in liquids: Given $D_S \sim 10^{-5}$ cm^2/s, as described in Sec. III B, Sc $\sim \mathcal{O}(10^3)$ in the present experiments.

Finally, the Stokes number of the sedimenting beacons here are $\mathcal{O}(0.1)$, taking the inertial time to be

$$\tau_I = \frac{2}{9}\frac{\rho_B R_B^2}{\mu}, \tag{5}$$

about 5 ms, and the flow time to be set by the time for the beacon to fall its own radius,

$$\tau_f = \frac{R_B}{U_B}, \tag{6}$$

about 40 ms. Stokes numbers for the suspended particles of size $R_p \sim \mathcal{O}(1\ \mu\mathrm{m})$ responding to the flow around the sedimenting beacon are smaller by a factor of order $(R_p/R_B)^2 \sim 10^{-4}$.

Figure 3 shows the sedimenting velocities of ionogel beacons with different sizes, where points show the experimentally derived velocities, while the line represents predictions from Eq. (1). The experimental measurements show good agreement with theory, using $\Delta\rho = 154$ kg/m^3 in Eq. (1) as the only fitting parameter.

Figures 4(a)–4(f) shows a time series of images of an ionogel beacon ($R_B = 0.35$ mm) that sediments through a suspension of negatively charged PS colloids. After sedimenting 12 mm in approximately 0.6 s, the [C$_4$mim][I] wake left by the beacon attracts particles from the

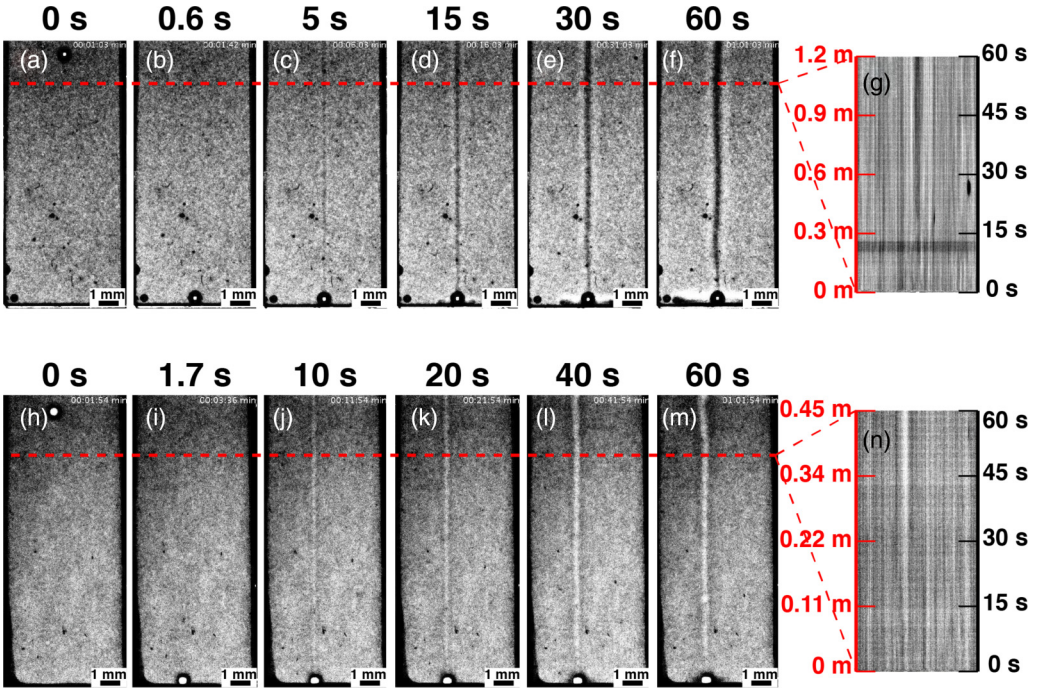

FIG. 4. Falling beacons loaded with the ionic liquid [C_4mim][I] [(a)–(g)] and the surfactant SDS [(h)–(n)] create wakes that attract and repel particles, respectively. Images show snapshots in time for each of the two beacons. (a) The [C_4mim][I] beacon enters the frame at $t = 0$ s and (b) hits the bottom of the container after 0.6 s; the wake diffuses out and collects particles, as seen after (c) 5 s, (d) 15 s, (e) 30 s, and (f) 60 s. (g) A pixel thick slice (at $z = 11.7$ mm), when stacked together, shows the temporal evolution of the particle concentration in the wake. The axis on the right shows the time elapsed after the beacon crosses the dashed red line in (f) and the axis on the left shows the distance the beacon would have fallen had the fluid been unbounded. The dark band between 12 and 13 s is an artifact of the illumination. (h) The SDS beacon enters at $t = 0$ s and (i) hits the bottom after 1.7 s. Unlike the ionic liquid, the SDS wake repels particles to create a depletion zone, as seen after (j) 10 s, (k) 20 s, (l) 40 s, and (m) 60 s. (n) A pixel thick slice (at $z = 8.6$ mm), when stacked together, shows the temporal evolution of the particle concentration in the wake. The axes on the left and right have the same interpretation as (g).

surrounding suspension, creating a relatively dark region where the particle concentration exceeds the background concentration ($N_{SI} > N_0$). Colloidal enrichment within the solute wake strengthens and grows appreciably during the subsequent minute.

Figure 4(g) shows the temporal evolution of the particle concentration within a single horizontal slice of the suspension, located 11.5 mm from the bottom of the sample cell, made by stacking the line of pixels at that height from each time. The axis on the right (black) shows the time elapsed after the beacon crosses the red dashed line (at 11.5 mm) in Figs. 4(a)–4(f). The axis on the left (red) shows the distance that the sedimenting ionogel beacon would have covered, had it continued to fall at its steady velocity of approximately 20 mm/s in an unbounded fluid. Figure 4(g) represents the steady-state particle enrichment profile viewed from a reference frame moving with the sedimenting beacon.

Figures 4(h)–4(m) show analogous experiments with a PEG-DA beacon loaded with SDS, which sediments more slowly (12.75 mm in approximately 1.7 s) due to its lower density. As expected, particles are repelled from the SDS wake, as indicated by the brighter streak in the center. Stacking horizontal slices [Fig. 4(n)] shows the particle distribution depleting over time at a single vertical

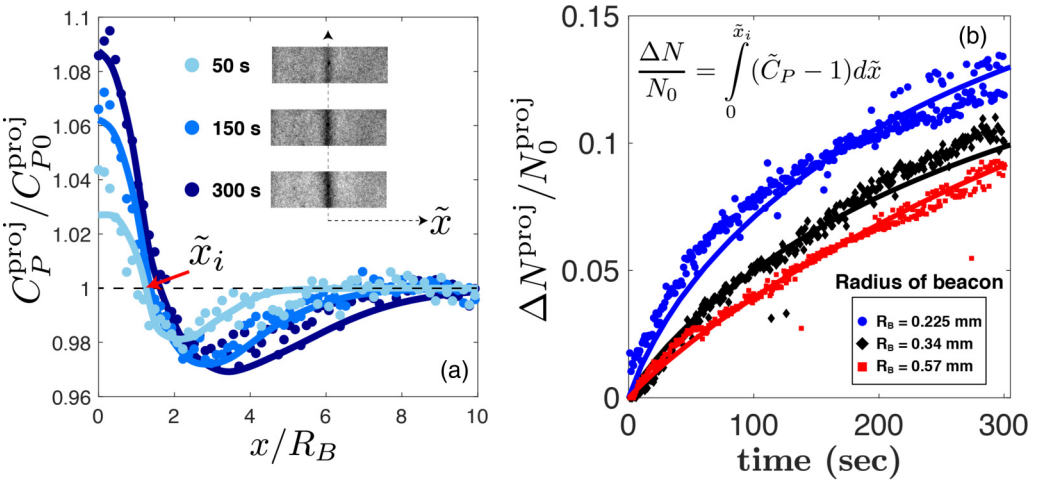

FIG. 5. Soluto-inertial attraction of suspended particles by the solute wake of a falling ionogel beacon leads to colloidal accumulation within the wake. (a) Projected concentration $C_P^{\mathrm{proj}}(x, z_0)$ at height z_0 in the sample cell, normalized by the background concentration $C_{P0}^{\mathrm{proj}}(x \to \infty)$ as a function of time. Particles migrate from the bulk suspension ($\tilde{x} > \tilde{x}_i$) to accumulate near the center of the solute wake ($\tilde{x} < \tilde{x}_i$), with intensity that increases over time. Lengths x are normalized by the beacon radius R_B, here 225 μm. Circle represent measured data points, and lines reflect predictions described in Sec. III. (b) The number $\Delta N(t)$ of particles collected by the solute wake increases with time, with a collection rate that decreases with beacon radius R_B. Theoretical predictions [Eqs. (23) and (9)] capture measured data.

position 9 mm from the bottom of the sample cell. The axes on the left and right have the same meaning as Fig. 4(g), with the left axis reflecting the shorter effective distance traveled due to the slower (7.5 mm/s) sedimentation velocity of the the SDS beacon.

The intensity of the light transmitted through the 3 mm deep sample cell is proportional to the number of particles along the line of sight at each pixel (Fig. 2), with the quantitative relation between (uniform) suspension concentration C_P and transmitted light intensity shown in the measured calibration curve (Fig. 11). Images in Fig. 4, and related experiments, reflect a two-dimensional (x-z) projection of a radially symmetric, three-dimensional particle distribution,

$$C_P^{\mathrm{proj}}(x, z) = \int_{y_l}^{y_r} C_P(x, y, z)dy, \tag{7}$$

which are determined using this calibration curve; $y_l = 0$ and $y_r = 3$ mm represent the left and right edges of the 3-mm-thick sample cell.

Figure 5(a) shows the projected particle concentration profile C_P^{proj} evolving in response to the [C_4mim][I] wake. As expected, colloids accumulate at the center of the solute wake. Since the total particle number is conserved, excess particles driven into the wake must be supplied by the neighboring regions of the suspension, necessitating particle depletion outside of the wake. Colloidal concentration thus transitions from a relative excess to a relative depletion at some distance x_i, determined experimentally, and ultimately recovers the bulk particle concentration far from the wake $x \gg x_i$. Experimental measurements (points) agree well with concentration profiles (lines) predicted theoretically, details of which are presented in Sec. III.

The rate with which particles are collected (or repelled) by the solute wake trailing behind a sedimenting soluto-inertial beacon depends on the radius R_B of the beacon. Figure 5(b) shows the projected excess number of particles collected within the wakes of sedimenting ionogel beacons

with three different radii. More specifically, the total projected excess number of particles,

$$\Delta N^{\text{proj}} = \int_{-x_i}^{x_i} \left(C_P^{\text{proj}} - C_{P0}^{\text{proj}}\right) dx, \tag{8}$$

reflects the excess projected particle concentration C_P^{proj} curves, integrated across the region of positive particle excess ($|x| < x_i$). Normalizing ΔN^{proj} by the number N_0^{proj} of "background" colloids that would have been in this excess region gives,

$$\Delta \tilde{N}^{\text{proj}} = \frac{\Delta N^{\text{proj}}}{N_0^{\text{proj}}} = \frac{\int_0^{x_i} \left[C_P^{\text{proj}}(x) - C_{P0}^{\text{proj}}\right] dx}{\int_0^{x_i} C_{P0}^{\text{proj}} dx}. \tag{9}$$

In dimensionless units, the projected excess collected becomes simply

$$\Delta \tilde{N}^{\text{proj}} = \int_0^{\tilde{x}_i} \left[\tilde{C}_P^{\text{proj}}(\tilde{x}) - 1\right] d\tilde{x}. \tag{10}$$

Filled points in Fig. 5(b) show $\Delta \tilde{N}^{\text{proj}}$ as it grows in time for sedimenting ionogel beacons of three different radii R_B, measured directly from experiments. These experimental results are captured well by theoretical predictions [lines in Fig. 5(b)] which follow from numerical computations of the fluid flows, solute transport, and diffusiophoretic particle migration, described immediately below.

III. THEORY

A predictive theory for the SI interactions driven by a sedimenting beacon must capture three basic ingredients: (i) the convective-diffusive transport of solute out of the SI beacon, here assumed to form a wake behind the sedimenting beacon; (ii) the radially diffusive relaxation of the solute wake far behind the beacon, where the fluid is largely stationary; and (iii) the diffusiophoretic migration of colloids in response to the radial solute flux. In all experiments discussed above, SI beacons fall fast enough that the timescales of these processes are well separated. In other words, beacon sedimentation is so fast that its solute wake persists long after the beacon has passed (and its associated flow has decayed). Moreover, the diffusive flux of solute away from the wake is largely radial and unaffected by the presence (or diffusiophoretic migration) of the dilute colloids in suspension. We therefore treat these stages separately. First, we analyze the convective-diffusive transport of solute emitted by the sedimenting SI beacon and its advection to form a solute wake trailing the beacon. Second, we treat the slow relaxation of the solute wake "far" behind the sedimenting beacon, where the fluid is stagnant and solute transport is almost entirely diffusive. Finally, we analyze the particle concentration field C_P as colloids migrate diffusiophoretically in response to the solute flux and diffusively.

A. Solute wake formation behind a sedimenting beacon

We first solve for the solute concentration profile in the comoving frame, so that the falling beacon remains at the origin and fluid in the far field moves with uniform velocity $-U_B\hat{\mathbf{z}}$, equal and opposite to the beacon sedimentation velocity U_B. Fluid flow past the beacon is assumed to be fully developed and laminar, obeying

$$\tilde{\nabla}^2 \tilde{\boldsymbol{u}} - \tilde{\nabla}\tilde{p} - \text{Re}\,(\tilde{\boldsymbol{u}} \cdot \tilde{\nabla}\tilde{\boldsymbol{u}}) = 0, \tag{11}$$

$$\tilde{\nabla} \cdot \tilde{\boldsymbol{u}} = 0, \tag{12}$$

where Re is the Reynolds number given by Eq. (2). The velocity field $\boldsymbol{u} = U_B\tilde{\boldsymbol{u}}$ is nondimensionalized by the beacon sedimentation velocity U_B, pressure $p = \tilde{p}\mu U_B/R_B$ by the viscous pressure scale, and radial $r = R_B\tilde{r}$ and axial $z = R_B\tilde{z}$ distances by the beacon radius. No-slip boundary conditions

are imposed at the beacon interface [$\tilde{\boldsymbol{u}}(\tilde{r}=1)=0$], while uniform flow velocity [$\tilde{\boldsymbol{u}}(\tilde{r}\to\infty)=-\hat{\boldsymbol{z}}$] is imposed far from the beacon.

Solute emitted from the beacon is advected by the fluid flow, obeying

$$\tilde{\nabla}^2\tilde{C}_S - \mathrm{Pe}\,(\tilde{\boldsymbol{u}}\cdot\tilde{\nabla}\tilde{C}_S)=0, \tag{13}$$

where solute concentration $C_S = C_0\tilde{C}_S$ is nondimensionalized by a characteristic solute concentration C_0, and the Peclet number Pe is defined by Eq. (3). The SI beacon is assumed to maintain a concentration C_0 in the fluid immediately adjacent to the beacon surface, so that $\tilde{C}_S(\tilde{r}=1)=1$, and the fluid is assumed to be solute-free in the far field [$\tilde{C}_S(\tilde{r}\to\infty)=0$].

In all experiments reported here, beacons fall fast enough that $\mathrm{Pe}\gg 1$, representing a limit in which outfluxed solute is expected to form thin convection-diffusion boundary layers around the beacon. Moreover, the fluid velocity immediately adjacent to the (no-slip) beacon surface has a predominantly shear character where the solute boundary layer is located. The thickness δ of the mass transport boundary layer should therefore follow Lévêque, or Prandtl-Blasius-Pohlhausen, scaling [18–20],

$$\delta = R_B\mathrm{Pe}^{-1/3}. \tag{14}$$

The total number of solute molecules leaving the beacon per unit time can thus be approximated as

$$J \sim \frac{4\pi R_B^2 D_S \Delta C_S}{\delta} \approx 4\pi R_B^2 D_S \frac{C_0}{\delta}. \tag{15}$$

The beacon sediments with velocity U_B. Thus, in time $t = l/U_B$, the outflux J is focused into a solute wake, with total solute mass M given by

$$M \approx J\frac{l}{U_B}. \tag{16}$$

From Eqs. (14)–(16), the solute mass per unit length λ can then be expressed as

$$\lambda = \frac{M}{l} = \frac{J}{U_B} \approx \frac{4\pi R_B^2 D_S C_0}{R_B\mathrm{Pe}^{-1/3}U_B} \approx 4\pi R_B^2 C_0 \mathrm{Pe}^{-2/3}. \tag{17}$$

Nondimensionalizing λ in Eq. (17) by $4\pi R_B^2 C_0$ gives

$$\tilde{\lambda} = \frac{\lambda}{4\pi R_B^2 C_0} \sim \mathrm{Pe}^{-2/3}. \tag{18}$$

COMSOL solutions to Eqs. (11)–(13) indeed verify the $\mathrm{Pe}^{-2/3}$ scaling, as found by integrating the solute at a fixed distance $\Delta z = 10R_B$ behind the beacon:

$$\lambda = 2\pi\int_0^\infty C_S(r, z=10R_B)\,r\,dr, \tag{19}$$

or its nondimensional analog,

$$\tilde{\lambda} = \frac{\lambda}{4\pi R_B^2 C_0} = \frac{1}{2}\int_0^\infty \tilde{C}_S(\tilde{r}, \tilde{z}=10)\,\tilde{r}\,d\tilde{r}. \tag{20}$$

Note that the location $\tilde{z}=10$ in the computations where $\tilde{\lambda}$ is calculated is arbitrary, since conservation requires the solute mass per unit length to be independent of the location behind the beacon. Figure 6 shows good agreement between the computed values of $\tilde{\lambda}$ (points) and the $\mathrm{Pe}^{-2/3}$ scaling predicted by Eq. (18) (line) for $1 < \mathrm{Pe} < 10^5$. The computations presented in Fig. 6 are performed in the Stokes flow regime with $\mathrm{Re}=0$, although finite Re has little effect, as discussed later.

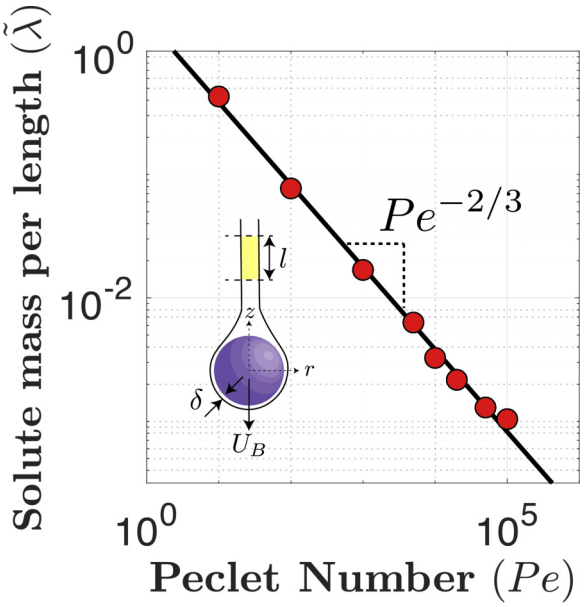

FIG. 6. The dimensionless total mass of solute collected in the trailing wake of a sedimenting beacon, per unit length of the wake. Points show numerically computed values of dimensionless mass per length vs Pe [Eq. (20)], while the solid line represents the $\mathrm{Pe}^{-2/3}$ scaling derived in Eq. (17). Computations are performed in the Stokes flow regime with $\mathrm{Re} = 0$.

B. DP response of suspended particles to the solute flux

The SI migration of colloids occurs over several minutes, whereas the beacon falls within a few seconds. Therefore, once the beacon falls far enough, the fluid can be considered to be largely stagnant. In the absence of flow, solute in the wake diffuses radially out according to

$$\frac{\partial \tilde{C}_S}{\partial \tilde{t}} - \tilde{\nabla}^2 \tilde{C}_S = 0, \tag{21}$$

where time is nondimensionalized by the solute diffusion time scale $t = R_B^2/D_S\tilde{t}$.

The particle concentration C_P in the suspension then evolves under this solute concentration gradient, as the particles migrate diffusiophoretically with velocity [21–23]

$$\boldsymbol{u}_{\mathbf{DP}} = D_{\mathrm{DP}} \nabla \ln C_S, \tag{22}$$

where D_{DP} is the DP mobility, whose sign and magnitude depends on the nature of the solute-particle interaction. Particles diffuse and move diffusiophoretically, obeying

$$\frac{\partial \tilde{C}_P}{\partial \tilde{t}} - \tilde{D}_P \tilde{\nabla}^2 \tilde{C}_P + \tilde{D}_{\mathrm{DP}} \tilde{\nabla} \cdot (\tilde{C}_P \tilde{\nabla} \ln \tilde{C}_S) = 0. \tag{23}$$

Two additional dimensionless parameters emerge from Eq. (23): the ratio of particle to solute diffusivity

$$\tilde{D}_P = \frac{D_P}{D_S}, \tag{24}$$

and the ratio of the DP mobility to the solute diffusivity,

$$\tilde{D}_{\mathrm{DP}} = \frac{D_{\mathrm{DP}}}{D_S}. \tag{25}$$

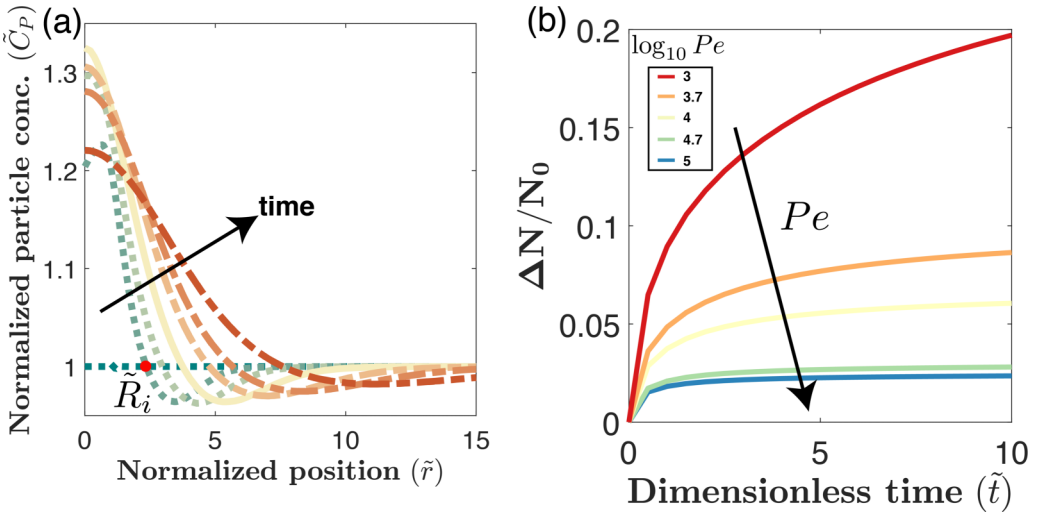

FIG. 7. Particle response to the solute wake established by a falling beacon that attracts colloids. (a) Evolution of particle concentration in suspension after the formation of the wake. Dotted teal lines show the initial increase in the particle concentration, until it reaches a maximum value at $t_{\max}$. This maximum concentration profile is shown by the solid yellow line. The concentration relaxes as the DP velocity diminishes and the particles diffuse out, which is shown by the dashed orange lines. The concentration profiles are calculated with $\tilde{D}_{\rm DP} = 10^{-1}$, the order of magnitude appropriate for the experiments, but with an unrealistically large particle diffusivity $\tilde{D}_P = 10^{-1}$ to match the strengths of the particle diffusive flux and the DP flux and therefore show their competition. (b) Excess particles ($\Delta N = N_{\rm SI} - N_0$) collected by the wake of sedimenting beacons vs Pe. Computations for the excess particles are performed with more realistic particle diffusivity $\tilde{D}_P = 10^{-4}$ and $\tilde{D}_{\rm DP} = 10^{-1}$, as appropriate for these experiments.

The Stokes-Einstein diffusivity, D_P of a 1-μm-radius particle in the glycerol-water mixture used in our experiments is approximately 0.1 $\mu{\rm m}^2/{\rm s}$. The diffusion coefficient of the ionic liquid in water, D_S, is around 1000 $\mu{\rm m}^2/{\rm s}$ [24], while for SDS it is around 800 $\mu{\rm m}^2/{\rm s}$ [25] at room temperature, meaning $\tilde{D}_P \sim 10^{-4}$ in our experiments. The magnitude of the DP mobility, $D_{\rm DP}$, under electrolyte and surfactant gradients typically ranges between 50 and 350 $\mu{\rm m}^2/{\rm s}$ [26,27]; taking 100 $\mu{\rm m}^2/{\rm s}$ as a typical order of magnitude in Fig. 7 gives $\tilde{D}_{\rm DP} \sim 0.1$. When comparing with experiments (e.g., Fig. 5) the specific value $\tilde{D}_{\rm DP} = 0.2$ gives a slightly better fit.

The particle concentration profile is obtained by solving Eqs. (21) and (23) and is shown in Fig. 7(a). As soon as solute starts diffusing out from the wake, a radial concentration gradient is established, which causes the particles to migrate via DP. Initially, solute concentration gradients (∇C_S) are sharp, so $\nabla \ln C_S$ is large enough that the DP flux ($\boldsymbol{u}_{\rm DP} C_P$) is much greater than the diffusive particle flux ($D_{\rm DP} \nabla C_P$). Thus, the particle concentration in the center of the wake initially increases [assuming DP migration to be directed up the gradient, dotted teal lines in Fig. 7(a)]. Over time, $\nabla \ln C_S$ weakens as solute diffuses out; at some time $t_{\max}$, particle diffusion starts to outcompete $\boldsymbol{u}_{\rm DP}$, and the particle accumulation spreads [dashed orange lines in Fig. 7(a)]. Eventually, the particle population relaxes back to its equilibrium uniform distribution (not shown). The computations presented in Fig. 7(a) are performed with $\tilde{D}_{\rm DP} = \tilde{D}_P = 10^{-1}$ to highlight the competition between the DP flux and the diffusive particle flux. Note, however, that $\tilde{D}_{\rm DP} \gg \tilde{D}_P$ for the systems of interest here.

The excess number of particles ($\Delta N = N_{\rm SI} - N_0$) collected behind the sedimenting beacon can be computed from the particle concentration profile C_P via

$$\Delta N = 2\pi \int_0^{R_i} [C_P(r) - C_{P0}] r dr, \tag{26}$$

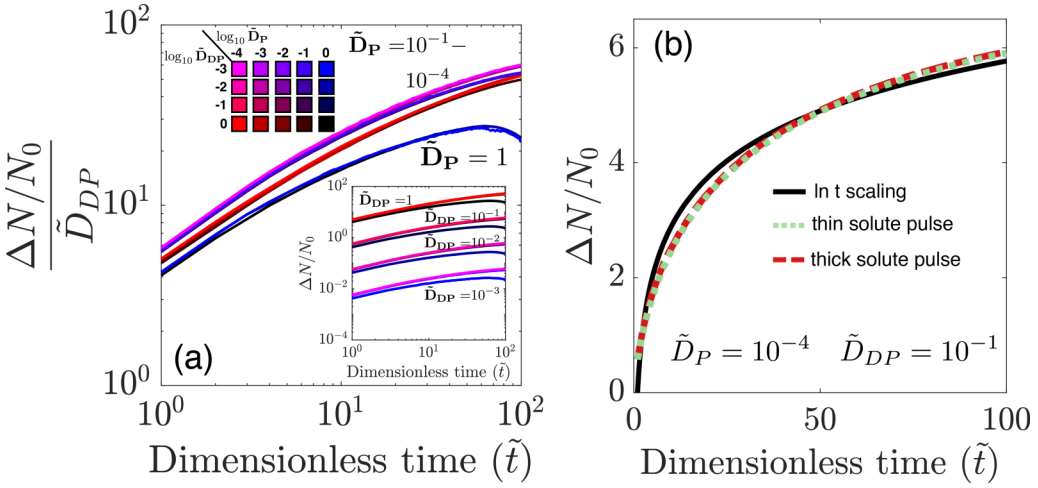

FIG. 8. Effect of particle diffusivity ($\tilde{D}_P$) and DP mobility ($\tilde{D}_{\rm DP}$) on colloidal collection in the beacon wake. (a) Excess particles collected in the wake ($\Delta N = N_{\rm SI} - N_0$), due to their DP migration toward higher solute concentration vs nondimensional time. The different curves collapse when scaled by the dimensionless DP mobility ($\tilde{D}_{\rm DP}$). Inset shows the raw, unscaled results. (b) Maintaining a constant mass of solute yet changing the width of the initial solute pulse does not impact the number of particles collected, shown by the dashed red and dotted green lines. Moreover, the increase in particle count follows a logarithmic scaling in time (black curve). Time is nondimensionalized by solute diffusion timescale, R_B^2/D_S.

integrating to the boundary R_i of the enriched region. Without DP, the particle concentration everywhere in the suspension would remain C_{P0}, and ΔN would remain zero. For reference, ΔN is normalized by the equivalent number N_0 of particles swept by the sedimenting beacon,

$$N_0 = 2\pi \int_0^{R_B} C_{P0} r dr = \pi R_B^2 C_{P0}, \tag{27}$$

to obtain

$$\frac{\Delta N}{N_0} = \Delta\tilde{N} = 2\int_0^{\tilde{R}_i} [\tilde{C}_P(\tilde{r}) - 1]\tilde{r} d\tilde{r}. \tag{28}$$

Computed values of the normalized excess particles collected in the wake ($\Delta\tilde{N}$) vs time [Fig. 7(b)] reveal $\Delta\tilde{N}$ to decrease with increasing Pe or sedimenting beacon velocity U_B. To compare with experiments which measure projected particle concentrations, we compute $\Delta\tilde{N}^{\rm proj}$ according to Eq. (9), plotted in Fig. 5(b) (lines). Choosing $\tilde{D}_{\rm DP} = 2 \times 10^{-1}$ and $\tilde{D}_P = 10^{-4}$—well within the values expected—gives excellent agreement with the experimental results for all three beacon sizes.

C. The effect of DP mobility and particle diffusivity on colloidal collection

We now examine the effect of the relative diffusivity $\tilde{D}_P$ and scaled DP mobility $\tilde{D}_{\rm DP}$ on the particle collection in the wake for a fixed beacon size (or Pe). Since Pe is kept fixed and its choice can be arbitrary, details of the initial solute concentration profile in the wake are not important. Therefore, to simplify our computational model, we approximate the initial solute distribution in the wake with a step function [of unit height and width, such that $\tilde{\lambda} = 1/4$, Pe $\approx \mathcal{O}(20)$], which eventually diffuses into a Gaussian profile. Figure 8(a) shows computed values of the excess particle number $\Delta\tilde{N}$ [Eq. (28)] in the wake as a function of relative diffusivities $\tilde{D}_P$ and scaled DP mobility $\tilde{D}_{\rm DP}$. Normalizing this excess collection by the scaled DP mobility $\tilde{D}_{\rm DP}$ collapses the different curves for all combinations of $\tilde{D}_{\rm DP}$ and $\tilde{D}_P$, except in the physically unrealistic limit $\tilde{D}_P \sim \mathcal{O}(1)$. Without

fully solving the coupled system of Eqs. (21) and (23), we propose a simple scaling argument to capture this data collapse and predict the temporal evolution profile for the excess number of particles.

Integrating Eq. (23) radially over the region where there is an excess concentration of particles ($\Delta C_P > 0$) gives

$$\frac{\partial \Delta N}{\partial t} = 2\pi \frac{\partial}{\partial t} \int_0^{\tilde{R}_i} \Delta \tilde{C}_p \tilde{r} d\tilde{r} \tag{29}$$

$$= 2\pi \int_0^{\tilde{R}_i} \left\{ \tilde{D}_P \frac{1}{\tilde{r}} \frac{\partial}{\partial \tilde{r}} \left[\tilde{r} \frac{\partial}{\partial \tilde{r}} (1 + \Delta \tilde{C}_P) \right] - \tilde{D}_{\mathrm{DP}} \frac{1}{\tilde{r}} \frac{\partial}{\partial \tilde{r}} \left[\tilde{r} \frac{\partial}{\partial \tilde{r}} \ln \tilde{C}_S (1 + \Delta \tilde{C}_P) \right] \right\} \tilde{r} d\tilde{r}, \tag{30}$$

where $\Delta \tilde{C}_P = \tilde{C}_P - 1$ and $\Delta \tilde{C}_P = 0$ at $\tilde{r} = \tilde{R}_i$. Normalizing Eq. (30) by the number N_0 of particles swept by the sedimenting beacon [Eq. (27)] and simplifying yields

$$\frac{\partial}{\partial \tilde{t}} \frac{\Delta N}{N_0} = 2 \left[\tilde{D}_P \tilde{r} \frac{\partial}{\partial \tilde{r}} (1 + \Delta \tilde{C}_P) - \tilde{D}_{\mathrm{DP}} \tilde{r} \frac{\partial}{\partial \tilde{r}} \ln \tilde{C}_S (1 + \Delta \tilde{C}_P) \right]_{\tilde{r} = \tilde{R}_i}, \tag{31}$$

$$\frac{\partial \Delta \tilde{N}}{\partial \tilde{t}} = 2 \left(\tilde{D}_P \tilde{r} \frac{\partial \tilde{C}_P}{\partial \tilde{r}} - \tilde{D}_{\mathrm{DP}} \tilde{r} \frac{\partial}{\partial \tilde{r}} \ln \tilde{C}_S \right)_{\tilde{r} = \tilde{R}_i}. \tag{32}$$

Figure 12 compares the two terms on the right-hand side of Eq. (32) and reveals that the DP term always dominates the particle diffusion term, irrespective of the value of $\tilde{D}_{\mathrm{DP}}$ [for realistic cases with $\tilde{D}_P < \mathcal{O}(1)$]. Neglecting the diffusive term in Eq. (32) then yields

$$\frac{\partial \Delta \tilde{N}}{\partial \tilde{t}} \approx -2 \tilde{D}_{\mathrm{DP}} \tilde{r} \frac{\partial}{\partial \tilde{r}} \ln \tilde{C}_S \Big|_{\tilde{r} = \tilde{R}_i}. \tag{33}$$

Equation (33) predicts $\Delta \tilde{N}$ to be directly proportional to the normalized DP mobility $\tilde{D}_{\mathrm{DP}}$, as evidenced by the data collapse observed in Fig. 8(a). Furthermore, it is only in the physically unreasonable limit $\tilde{D}_P \sim \mathcal{O}(1)$ that the DP and particle diffusivity terms in Eq. (32) are of the same order of magnitude (Fig. 12), in which case the scaling does not work [Fig. 8(a)].

Equation (33) predicts the excess particles collected (or depleted) by the wake of a falling beacon, and requires the solute concentration profile C_S in solution to be known.

Computations [Fig. 8(b)] reveal that the total number of particles collected does not depend on the detailed solute profile, since thin wakes (green dotted line) collect the same particle excess $\Delta \tilde{N}$ as wide pulses (red dashed line) of same solute mass density $\tilde{\lambda}$. These computations are performed with $\tilde{D}_P = 10^{-4}$ and $\tilde{D}_{\mathrm{DP}} = 10^{-1}$, motivated by experimentally realistic conditions. Since the number of particles collected does not depend on the thickness of the solute pulse, the initial wake may be assumed to be infinitely thin. This assumption then allows the diffusive solute concentration profile in solution to be approximated as a Gaussian distribution, which in polar coordinates can be expressed as

$$C_S(r, t) = \frac{\lambda}{4\pi D_S t} \exp\left(-\frac{r^2}{4 D_S t} \right). \tag{34}$$

Using this approximation for C_S in Eq. (33) predicts

$$\Delta \tilde{N} \approx \tilde{D}_{\mathrm{DP}} \tilde{R}_i^2 \ln \tilde{t}. \tag{35}$$

Note that to arrive at Eq. (35), we made the assumption that the cutoff location R_i is independent of time. This approximation appears reasonable when colloidal diffusion is slow and the particle concentration relaxes gradually ($\tilde{D}_P < 1$). Figure 13 validates this approximation: tracking the evolution of $\tilde{R}_i$ over time reveals that it changes by less than 50% over 80 dimensionless times.

Two qualitative features emerge from the preceding scaling analysis. First, Eq. (35) predicts the excess number of particles in the wake ($\Delta N/N_0$) to be directly proportional to the scaled DP mobility $\tilde{D}_{\mathrm{DP}}$, which explains the data collapse observed in Fig. 8(a). Second, the particle count in the wake

is expected to increase logarithmically with time, as is indeed observed in the full computations. Figure 8(b) shows good agreement between the prediction from this logarithmic scaling (black curve) and the computed data (red and green lines). The small deviation from the logarithmic trend might reflect the slight drift in $\tilde{R}_i$ over time.

IV. MATERIALS AND METHODS

A. Sample cell fabrication

A 3-mm-thick piece of acrylic is cut with a computer-controlled laser cutter (Trotec Speedy 100) in the dimensions of the sample chamber (6 mm wide and 40 mm tall). The acrylic is sandwiched between two glass slides and the assembly is sealed with UV curable glue (NOA-81; Norland Adhesive). The cell is then covered with a glass cover slip with a hole drilled in the center to provide access.

B. Sample preparations

The ionogel precursor solution is prepared by mixing 32% (vol/vol) polyethylene glycol-diacrylate (PEG-DA) 700 (Sigma-Aldrich) with 66% (vol/vol) pure [C_4mim][I] (Sigma-Aldrich) and 2% (vol/vol) photoinitiator (2-hydroxy-2-methylpropiophenone; Sigma-Aldrich). A drop of the precursor solution is carefully injected into a 1000-csT silicone oil (Sigma-Aldrich) bath and immediately placed inside a UV oven for 1 min. The precursor drop cures under UV light into a spherical hydrogel, as it slowly falls down in the highly viscous oil bath. The polymerized gel (ionogel beacon) is subsequently scooped from the bottom of the bath and cleaned with a dry lens tissue.

The SDS gel precursor is prepared by mixing 32% (vol/vol) PEG-DA with an SDS stock solution and 2% (vol/vol) photoinitiator, such that the resultant SDS concentration in the precursor is 200 mM. Spherical beacons are then created following the same technique as the ionogel beacons.

Suspension of polystyrene (PS) particles is prepared by mixing 24% (vol/vol) glycerol (Thermo-Fisher) with 76% (vol/vol) deionized (DI) water and 0.025% (vol/vol) carboxylated (negatively charged), surfactant-free PS beads, 2 μm in diameter (Magsphere Inc. SFCA002UM).

C. Image recording and data analysis

The suspension is illuminated with a thin laser sheet (Laserland 11061123) and a zoom lens (Computar MLM-3XMP) attached to a high-speed camera (Ximea MQ013MG-ON) is used to record images from the bottom, at a frame rate of 100 frames/s, to obtain the image stack shown in Fig. 1(f). The center of the image [Fig. 1(f)] looks dark, because the fallen beacon at the bottom of the sample cell physically blocks the scattered light from the colloids to enter the camera.

Clamps are used to hold the sample cell in place and a zoom lens (Navitar Zoom 7000) attached to a CCD camera (Thorlabs DCU223M) is used to record images from the side, at a frame rate of 10 frames/s. A uniform, diffuse white light source is held behind the cell to maintain bright-field illumination throughout the experiment. Image recording is started and the beacon is gently introduced into the sample cell with a pair of tweezers.

A calibration curve is obtained for the transmitted light intensity captured by the camera vs particle concentration in the suspension (see Fig. 11). This calibration curve is subsequently used to obtain the particle distribution profiles from the bright-field images of the actual experiments. The excess amount of particles collected in the wake is then calculated numerically from the particle concentration profiles. The falling beacon velocity in Fig. 3 is calculated by measuring the frame by frame displacement of the beacon from the recorded images. These measurements are then averaged over all the frames where displacement is observed, except the one where the beacon hits the bottom of the sample cell. The error bars show the standard deviation in averaging. The size and the location of the beacon are directly approximated from the images, using the `imfindcircles` package on MATLAB.

D. COMSOL modeling

The `Laminar flow` and the `Transport of diluted species` modules in COMSOL Multiphysics are used to numerically solve the system of coupled differential equations (Eqs. 11, 12 and 13) in a 2D axisymmetric geometry. The computations are performed in the beacon's frame of reference; the beacon is kept fixed, while steady, fully developed fluid flow is imposed at the sedimenting beacon velocity (corresponding to different values of Pe) to obtain solute concentration profile in the wake at steady state. This solute wake profile is used as initial condition to solve Eqs. (21) and (23) using the `Transport of diluted species` and the `General form of PDE` modules, respectively, in a 1D axisymmetric geometry. Numerical solution to these equations reveals the particle distribution profile $\tilde{C}_P$. The Parametric Sweep option on COMSOL is used to perform computations for several permutations and combinations of the design parameters. Computed values of the solute and particle concentration profiles are subsequently exported in matrix form, which are postprocessed and analyzed on MATLAB. Additional details about the model are presented in the Appendix.

V. DISCUSSION

We have shown that the DP migration of suspended particles driven by the wake left behind a sedimenting beacon can be modeled by the separation of two timescales. One reflects the time to establish steady-state solute concentration profile in the wake, and the other over which transient solute diffusion occurs in the quiescent fluid. We also demonstrated that the particle transport in the wake's vicinity is a balance between particle diffusion and advection due to the diffusiophoretic migration of particles under the solute flux.

Equations (11)–(13) can predict the steady-state characteristics of the solute distribution in the wake of a beacon, moving with any arbitrary velocity U_B, and therefore are generally valid across all values of Re and Pe.

The total solute mass per unit length of the wake is expected to scale like $\mathrm{Pe}^{-2/3}$ [Eq. (17)]. Although the scaling analysis makes no assumption about the value of Re, the computations in Fig. 6 are performed in the Stokes flow limit, with $\mathrm{Re} = 0$. Figure 9 shows computations performed in the regime of inertially dominated momentum transport ($\mathrm{Re} > 0$). A remarkable conclusion that can be drawn from Fig. 9 is that the total solute mass collected in the wake remains independent of Re, depending only on Pe (at least in the limit of $0 \leqslant \mathrm{Re} \leqslant 100$). We therefore expect the $\mathrm{Pe}^{-2/3}$ dependence of $\tilde{\lambda}$ [Eq. (17)] to be generally valid across relevant values of Re, so long as the flow is steady and laminar, as shown by the solid black line in Fig. 9.

VI. CONCLUSION

Soluto-inertial beacons that establish long-lasting chemical gradients, can drive long-range diffusiophoretic migration of colloids. Although we had demonstrated the SI concept in fixed 2D microfluidic geometries, here we have shown that beacon additives can also drive long-range interactions in bulk, 3D suspensions. We specifically explored the high-Pe limit, where macroscopic beacons sediment within the suspension and their sedimenting velocity advects some amount of solute in the trailing wake. In this limit, the beacon sedimentation is fast, such that the solute in the wake subsequently diffuses out in a relatively stagnant fluid. This solute flux then drives the diffusiophoretic migration of nearby suspended objects. The total particle collection (or depletion) behind the falling beacon is a balance between the diffusiophoretic flux that drives particles into (or away from) the wake, and the diffusive flux that drives particles toward a uniform distribution.

We further envision slowly falling beacons in the low-Pe limit or even freely suspended beacons ($\mathrm{Pe} = 0$) to not only induce migration of passive particles in the suspension, but also interact with each other. Interactions between such "active beacons" would suggest interesting possibilities in 3D self assembly and autonomous propulsion, akin to the interactions between active materials on 2D planar surfaces reported previously [28–33].

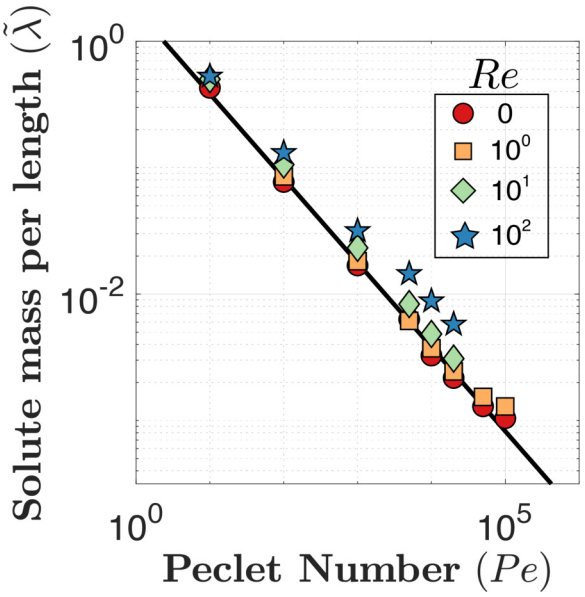

FIG. 9. Dimensionless total solute mass in the wake per unit length ($\tilde{\lambda}$), as a function of Pe, at different values of Re. Computations (points) reveal $\tilde{\lambda}$ to be independent of Re, scaling as $\mathrm{Pe}^{-2/3}$ (line), irrespective of Re.

ACKNOWLEDGMENTS

We gratefully acknowledge early support from the National Science Foundation (Grant No. CBET-1438779) and the Saudi Arabian Oil Company (Saudi Aramco, Contract No. A-0002-2018). Any opinion, findings, and conclusions or recommendations expressed in this material are those of the authors and do not necessarily reflect the views of the National Science Foundation. A portion of this work was performed in the Microfluidics Laboratory within the California NanoSystems Institute, supported by the University of California, Santa Barbara and the University of California, Office of the President, and in the shared facilities of the UCSB MRSEC (NSF DMR 1720256), a member of the Materials Research Facilities Network [34].

APPENDIX A: COMSOL COMPUTATION DETAILS

The beacon sedimentation, which occurs over relatively short timescales, is assumed to establish a quasi-steady-state solute distribution profile in the wake of the beacon. In a frame comoving with the beacon, the fully developed, steady-state fluid flow past the beacon obeys

$$\tilde{\nabla}^2\tilde{\boldsymbol{u}} - \tilde{\boldsymbol{\nabla}}\tilde{p} - \mathrm{Re}\,(\tilde{\boldsymbol{u}}\cdot\tilde{\boldsymbol{\nabla}}\tilde{\boldsymbol{u}}) = 0, \tag{A1}$$

$$\tilde{\boldsymbol{\nabla}}\cdot\tilde{\boldsymbol{u}} = 0. \tag{A2}$$

Re is the Reynolds number, which is directly tuned in the computations as a design parameter. The dimensionless Eqs. (A1) and (A2) are solved in a 2D axisymmetric geometry (Fig. 10) by imposing the following boundary conditions:

$$\tilde{\boldsymbol{u}} = 1\hat{\boldsymbol{e}}_z \quad \text{at the bottom ``inlet'' of the computational domain, } \tilde{z} = -100, \tag{A3}$$

$$\tilde{p} = 0 \quad \text{at the top ``outlet'' of the computational domain, } \tilde{z} = 100, \tag{A4}$$

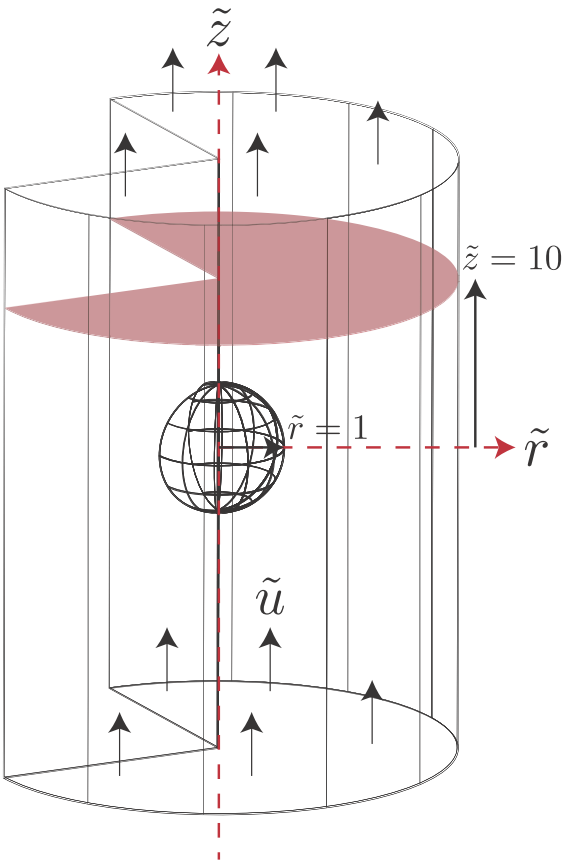

FIG. 10. 2D axisymmetric geometry, representative of the COMSOL computational domain used to solve Eqs. (A1)–(A10).

$$\tilde{\boldsymbol{u}} = 0 \quad \text{at the beacon-liquid interface,} \tag{A5}$$

$$\hat{\boldsymbol{n}} \cdot \tilde{\nabla} \tilde{\boldsymbol{u}} = 0 \quad \text{at } \tilde{r} = 0 \text{ and the "outer edge}'' \text{ of the computational domain,} \tag{A6}$$

where $\hat{\boldsymbol{e}}_z$ is the unit normal in the z direction, and $\hat{\boldsymbol{n}}$ is the outward unit normal on the respective boundaries. The solute leaving the beacon is advected by this fluid flow. At steady state, the solute concentration in the wake is solved according to

$$\tilde{\nabla}^2 \tilde{C}_S - \mathrm{Pe}\,(\tilde{\boldsymbol{u}} \cdot \tilde{\nabla} \tilde{C}_S) = 0, \tag{A7}$$

where Pe is the Peclet number, which is also tuned as one of the design parameters in the computations. The solute concentration is subject to the following boundary conditions:

$$\tilde{C}_S = 1 \quad \text{at the beacon-fluid interface,} \tag{A8}$$

$$\tilde{C}_S = 0 \quad \text{at the bottom "inlet}'' \text{ of the computational domain,} \tag{A9}$$

$$\hat{\boldsymbol{n}} \cdot \tilde{\nabla} C_S = 0 \quad \text{at } \tilde{r} = 0\,, \text{ at the top "outlet}'' \text{ and the "outer edge}'' \text{ of the computational domain.} \tag{A10}$$

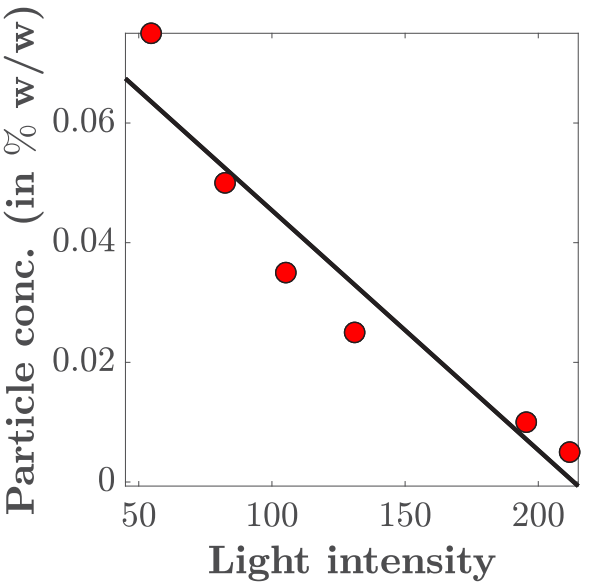

FIG. 11. A calibration curve is prepared to calculate the concentration of colloids in the suspension, as a function of the transmitted light intensity.

A 2D slice of the steady-state solute concentration profile in the wake at $\tilde{z} = 10$ (Fig. 10) is subsequently used as the initial condition to solve the transient solute diffusion in a stagnant fluid, according to

$$\frac{\partial \tilde{C}_S}{\partial \tilde{t}} - \tilde{\nabla}^2 \tilde{C}_S = 0. \tag{A11}$$

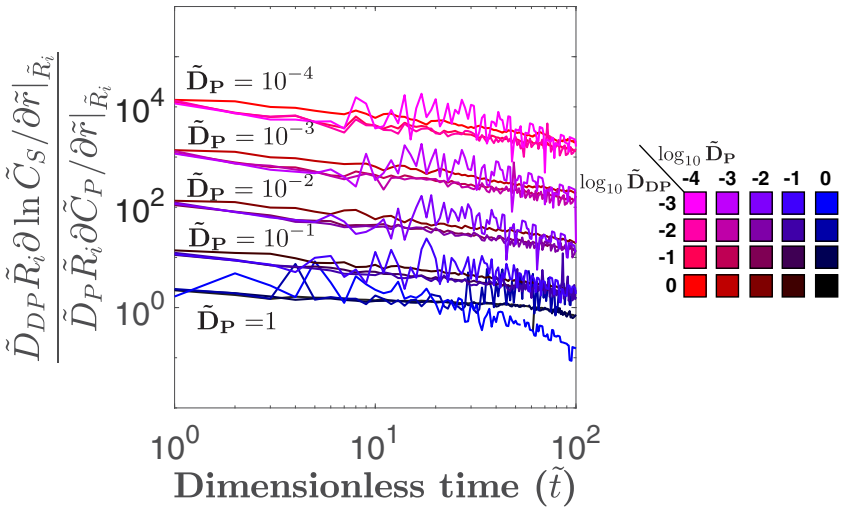

FIG. 12. Comparison between the strength of the diffusiophoretic particle flux driven by the solute wake ($\tilde{D}_{\mathrm{DP}}\tilde{R}_i\tilde{\nabla} \ln \tilde{C}_S|_{\tilde{R}_i}$) and the diffusive particle flux ($\tilde{D}_P\tilde{R}_i\tilde{\nabla}\tilde{C}_P|_{\tilde{R}_i}$), at different combinations of the scaled DP mobility $\tilde{D}_{\mathrm{DP}}$ and particle diffusivity $\tilde{D}_P$.

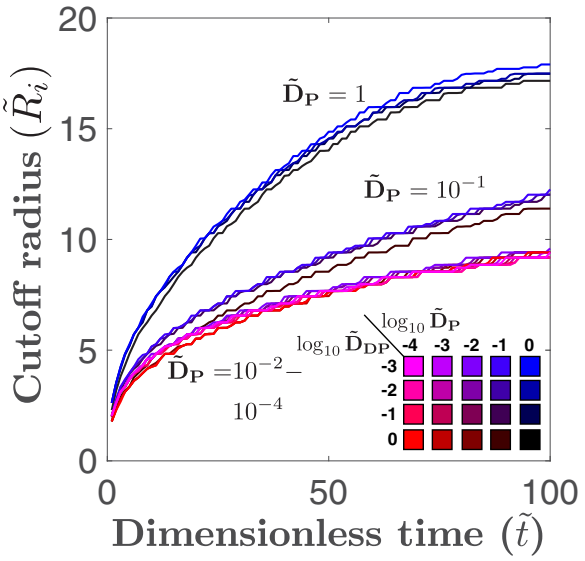

FIG. 13. Temporal evolution of the location $\tilde{R}_i$ beyond which, the excess particles in the center of the wake is balanced by a net depletion of particles in the suspension, at different combinations of the scaled DP mobility $\tilde{D}_{\mathrm{DP}}$ and particle diffusivity $\tilde{D}_P$.

This part of the problem is solved in a 1D axisymmetric geometry. The symmetry and no flux boundary conditions at the center and edges of the computational domain, respectively, imply

$$\hat{\boldsymbol{n}} \cdot \tilde{\boldsymbol{\nabla}} \tilde{C}_S = 0 \quad \text{at } \tilde{r} = 0, \text{ and the "outer edge."} \tag{A12}$$

Finally, this solute flux drives the diffusiophoretic migration of particles, which is balanced by particle diffusion according to

$$\frac{\partial \tilde{C}_P}{\partial \tilde{t}} - \tilde{D}_P \tilde{\nabla}^2 \tilde{C}_P + \tilde{D}_{\mathrm{DP}} \tilde{\boldsymbol{\nabla}} \cdot (\tilde{\boldsymbol{\nabla}} \ln \tilde{C}_S \, \tilde{C}_P) = 0. \tag{A13}$$

The scaled particle diffusivity $\tilde{D}_P$ and the scaled diffusiophoretic mobility $\tilde{D}_{\mathrm{DP}}$ are two independent design parameters and are tuned separately to perform computations for different combinations of the two. The following initial and boundary conditions are imposed on the particle concentration

$$\tilde{C}_P(\tilde{r}, \tilde{t} = 0) = 1 \tag{A14}$$

$$\hat{\boldsymbol{n}} \cdot \tilde{\boldsymbol{\nabla}} \tilde{C}_P = 0 \quad \text{at } \tilde{\mathrm{r}} = 0, \text{ and the "outer edge."} \tag{A15}$$

APPENDIX B: LIGHT INTENSITY VERSUS PARTICLE CONCENTRATION CALIBRATION

Red points in Fig. 11 show the measured values of particle concentration (reported as % wt/wt solids in the glycerol-water mixture) versus the light intensity recorded in the digital images where 0 is black and 255 is white. A straight line is fit through the measured points and is used to calculate the concentration of colloids in the suspension from the recorded grayscale images (like the ones shown in Fig. 4).

APPENDIX C: ASSUMPTIONS LEADING TO ANALYTICAL EXPRESSION FOR THE EXCESS PARTICLE COLLECTION ΔN

Equation (35) provides an analytical expression for the excess number of particles collected in the wake of a falling beacon $\Delta\tilde{N}$. This expression is derived by simplifying the equation for the rate of change of $\Delta\tilde{N}$ which in its most general form is given by Eq. (32). The simplification of Eq. (32) involves two assumptions. First, the contribution of DP migration of particles leading to the excess $\Delta\tilde{N}$ [second term on the right-hand side of Eq. (32)] is assumed to be greater than the diffusive smoothing of particles [first term on the right-hand side of Eq. (32)]. This assumption holds in the physically realistic limit of $\tilde{D}_P \ll 1$ as shown in Fig. 12.

Second, the cutoff location $\tilde{R}_i$ where the particle concentration transitions from a relative excess to a relative depletion is assumed to be independent of time. Figure 13 shows that although $\tilde{R}_i$ is not entirely constant, it only changes by less than 50% once it is established (after about 20 dimensionless times). This assumption also holds in the limit of $\tilde{D}_P \ll 1$.

[1] E. Dickinson, Colloids in food: Ingredients, structure, and stability, Annu. Rev. Food Sci. Technol. **6**, 211 (2015).

[2] G. Maitland, Transforming "formulation": Systematic soft materials design, Soft Matter. **1**, 93 (2005).

[3] L. Goehring, J. Li, and P. C. Kiatkirakajorn, Drying paint: From micro-scale dynamics to mechanical instabilities, Phil. Trans. R. Soc. A. **375**, 20160161 (2017).

[4] P. L. Saldanha, V. Lesnyak, and L. Manna, Large scale syntheses of colloidal nanomaterials, Nano Today **12**, 46 (2017).

[5] C. Majidi, Soft robotics: A perspective—Current trends and prospects for the future, Soft Robot. **1**, 5 (2014).

[6] R. L. Truby and J. A. Lewis, Printing soft matter in three dimensions, Nature **540**, 371 (2016).

[7] J. N. Israelachvili, *Intermolecular and Surface Forces*, 3rd ed. (Academic Press, San Diego, CA, 2011).

[8] V. G. Levich, *Physicochemical Hydrodynamics*, Prentice-Hall International Series in the Physical and Chemical Engineering sciences (Prentice-Hall, Upper Saddle River, NJ, 1962).

[9] D. Lohse and X. Zhang, Physicochemical hydrodynamics of droplets out of equilibrium: A perspective review, arXiv:2005.03782 (2020).

[10] S. Marbach and L. Bocquet, Osmosis, from molecular insights to large-scale applications, Chem. Soc. Rev. **48**, 3102 (2019).

[11] D. Velegol, A. Garg, R. Guha, A. Kar, and M. Kumar, Origins of concentration gradients for diffusiophoresis, Soft Matter **12**, 4686 (2016).

[12] A. Banerjee, I. Williams, R. N. Azevedo, M. E. Helgeson, and T. M. Squires, Soluto-inertial phenomena: Designing long-range, long-lasting, surface-specific interactions in suspensions, Proc. Natl. Acad. Sci. USA **113**, 8612 (2016).

[13] A. Banerjee and T. M. Squires, Long-range, selective, on-demand suspension interactions: Combining and triggering soluto-inertial beacons, Sci. Adv. **5**, eaax1893 (2019).

[14] A. Banerjee, D. R. Vogus, and T. M. Squires, Design strategies for engineering soluto-inertial suspension interactions, Phys. Rev. E **100**, 052603 (2019).

[15] J. L. Anderson, Colloid transport by interfacial forces, Ann. Rev. Fluid Mech. **21**, 61 (1989).

[16] T. M. Squires, *Particles in Electric Fields* (John Wiley & Sons, New York, 2016), pp. 59–79.

[17] A. Volk and C. J. Kähler, Density model for aqueous glycerol solutions, Exp. Fluids **59**, 75 (2018).

[18] L. G. Leal, *Advanced Transport Phenomena: Fluid Mechanics and Convective Transport Processes*, Cambridge Series in Chemical Engineering (Cambridge University Press, Cambridge, UK, 2007). Available from: https://books.google.com/books?id=jbRGKo1IeOwC.

[19] M. A. Lévêque, Les lois de la transmission de chaleur par convection, Ann. Mines: Mem. **12**, 201 (1928).

[20] H. Schlichting and K. Gersten, *Boundary-Layer Theory, Physic and Astronomy* (Springer, Berlin, 2003).

[21] D. C. Prieve, Migration of a colloidal particle in a gradient of electrolyte concentration, Adv. Colloid Interface Sci. **16**, 321 (1982).
[22] D. C. Prieve, J. L. Anderson, J. P. Ebel, and M. E. Lowell, Motion of a particle generated by chemical gradients. Part 2. Electrolytes, J. Fluid Mech. **148**, 247 (1984).
[23] J. L. Anderson and D. C. Prieve, Diffusiophoresis: Migration of colloidal particles in gradients of solute concentration, Separation and Purification Reviews **13**, 67 (1984).
[24] S. Sarraute, M. F. Costa Gomes, and A. A. H. Pádua, Diffusion coefficients of 1-alkyl-3-methylimidazolium ionic liquids in water, methanol, and acetonitrile at infinite dilution, J. Chem. Eng. Data **54**, 2389 (2009).
[25] R. M. Weinheimer, D. F. Evans, and E. L. Cussler, Diffusion in surfactant solutions, J. Colloid Interface Sci. **80**, 357 (1981).
[26] R. Nery-Azevedo, A. Banerjee, and T. M. Squires, Diffusiophoresis in ionic surfactant gradients, Langmuir **33**, 9694 (2017).
[27] J. S. Paustian, C. D. Angulo, R. Nery-Azevedo, N. Shi, A. I. Abdel-Fattah, and T. M. Squires, Direct measurements of colloidal solvophoresis under imposed solvent and solute gradients, Langmuir **31**, 4402 (2015).
[28] B. Liebchen, R. Niu, T. Palberg, and H. Löwen, Unraveling modular microswimmers: From self-assembly to ion-exchange-driven motors, Phys. Rev. E **98**, 052610 (2018).
[29] P. G. Moerman, H. W. Moyses, E. B. van der Wee, D. G. Grier, A. van Blaaderen, W. K. Kegel, J. Groenewold, and J. Brujic, Solute-mediated interactions between active droplets, Phys. Rev. E **96**, 032607 (2017).
[30] R. Niu, T. Palberg, and T. Speck, Self-Assembly of Colloidal Molecules due to Self-Generated Flow, Phys. Rev. Lett. **119**, 028001 (2017).
[31] R. Niu, D. Botin, J. Weber, A. Reinmüller, and T. Palberg, Assembly and speed in ion-exchange-based modular phoretic microswimmers, Langmuir **33**, 3450 (2017).
[32] I. Theurkauff, C. Cottin-Bizonne, J. Palacci, C. Ybert, and L. Bocquet, Dynamic Clustering in Active Colloidal Suspensions with Chemical Signaling, Phys. Rev. Lett. **108**, 268303 (2012).
[33] J. Palacci, S. Sacanna, A. P. Steinberg, D. J. Pine, and P. M. Chaikin, Living crystals of light-activated colloidal surfers, Science **339**, 936 (2013).
[34] www.mrfn.org.